High-Fidelity Meshing and Stochastic Simulation for Enhanced Surface Stress Concentration Prediction

IOP Conference Series:
Materials Science and
Engineering



**PAPER** • **OPEN ACCESS**

# High-Fidelity Meshing and Stochastic Simulation for Enhanced Surface Stress Concentration Prediction

To cite this article: Davide Angelini *et al* 2025 *IOP Conf. Ser.: Mater. Sci. Eng.* **1338** 012011



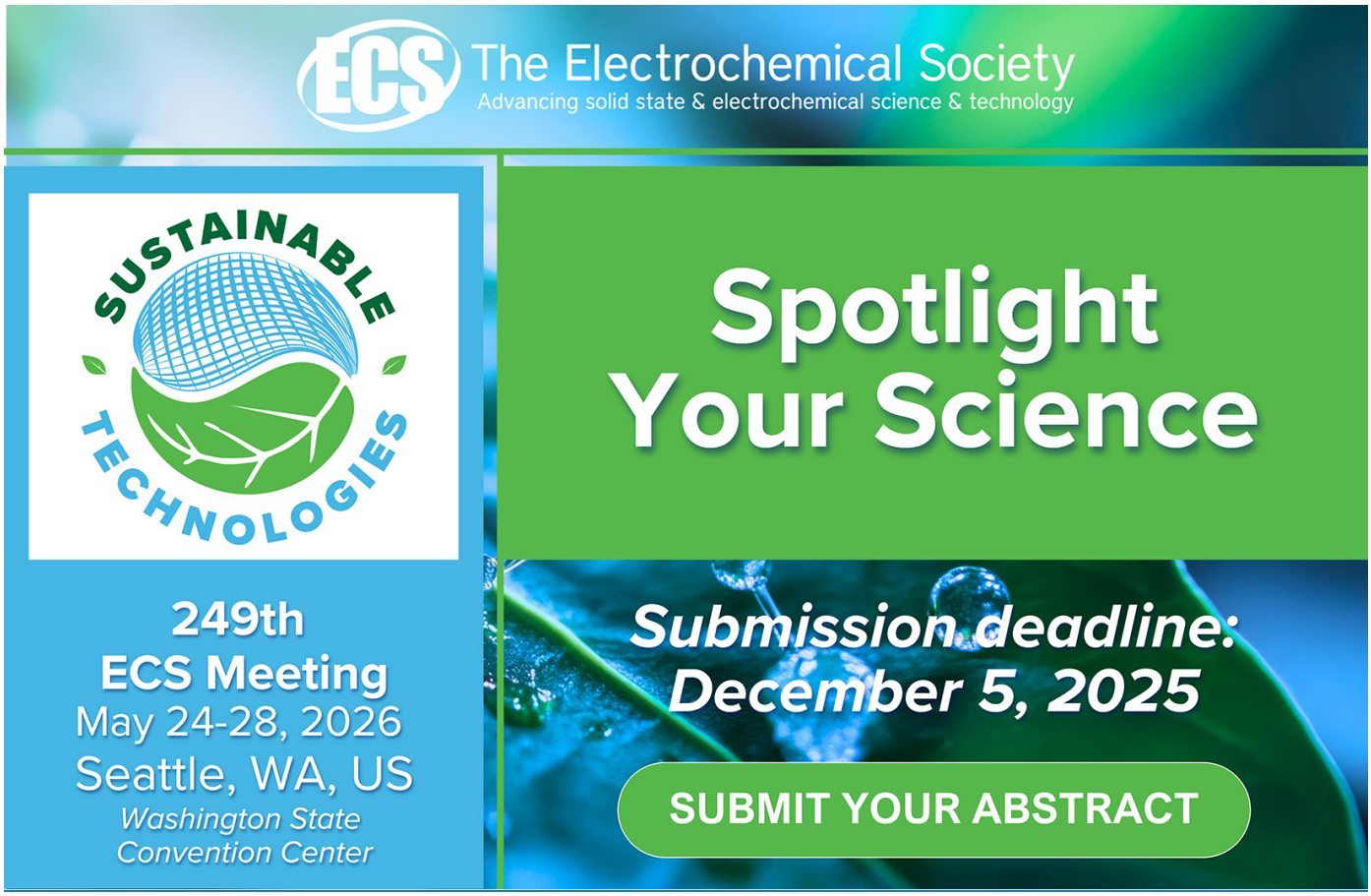

IOP Conf. Series: Materials Science and Engineering **1338** (2025) 012011 doi:10.1088/1757-899X/1338/1/012011

# High-Fidelity Meshing and Stochastic Simulation for Enhanced Surface Stress Concentration Prediction

**Davide Angelini[1], Enrico Cestino[1], Sergio Bianco[2] and Fabio Mallamo[2]**

[1]DIMEAS - Department of Mechanical and Aerospace Engineering, Politecnico di Torino, Corso Duca degli Abruzzi 24, Turin, 10129, TO, Italy
[2]FEV Italia s.r.l., Environment Park – Parco Scientifico Tecnologico per l'Ambiente, Via Livorno, 60, Turin, 10144, TO, Italy

Contact address: davide.angelini@polito.it

**Abstract.** The accurate prediction of the Stress Concentration Factor ($K_t$) induced by surface topography is critical for the fatigue life assessment of engineering components. Existing models, such as the semi-empirical model by Arola-Ramulu, offer methods to estimate $K_t$, but their accuracy varies with material and roughness characteristics. This study presents a systematic evaluation of these established models using a robust stochastic simulation framework. A computational workflow is developed in Python, integrating a surrogate-based optimization algorithm with the *Gmsh* library to ensure the generation of high-fidelity Finite Element meshes for 2D dog-bone specimens. A large-scale numerical campaign is conducted on specimens made of aluminum alloy and steel, featuring statistically generated random roughness profiles. The roughness parameters for each specimen were catalogued, and the corresponding $K_t$ is determined via linear elastic Finite Element Analysis (FEA) using Altair OptiStruct.The results from the FEA were directly compared against the predictions from Arola's rule and Zhang's Bayesian model. The analysis confirms that while Arola's rule provides reasonable estimates for low levels of roughness, it significantly underestimates $K_t$ for more severe surface topographies. In contrast, Zhang's model demonstrated superior predictive accuracy across a wider range of roughness conditions for both materials investigated. The findings highlight that a stochastic FEA approach, underpinned by high-fidelity meshing, is an effective method for validating and comparing surface stress concentration models. The results indicate that Zhang's model is a more reliable choice for general engineering applications. Future work should extend this framework to include material plasticity, 3D surface topographies, and validation against experimentally measured surface profiles.

## 1 Introduction

The fatigue life of a mechanical component is fundamentally influenced by its material properties, geometric configuration, and the applied loading path. A key parameter in fatigue analysis is the theoretical Stress Concentration Factor, denoted as $K_t$. This factor quantifies the localized increase in stress due to geometric discontinuities, such as notches or holes, relative to the nominal stress state [1]:

$$K_t = \frac{\sigma_{\text{peak}}}{\sigma_{\text{nominal}}} \tag{1}$$

where $\sigma_{\text{peak}}$ is the maximum local stress at the discontinuity and $\sigma_{\text{nominal}}$ is the stress in the region unaffected by the discontinuity. The magnitude of $K_t$ serves as a critical indicator of fatigue performance, as higher values correspond to an increased probability of crack initiation.

Numerous researchers have contributed to the compilation and calculation of $K_t$ values for various geometries and loading conditions. Peterson's work [2] remains a comprehensive resource, providing a vast collection of stress concentration factors for metallic structures derived from both analytical and numerical methods. A classic example is the case of an infinite plate with a central circular hole under

uniaxial tension, for which the analytical solution yields $K_t = 3$. This result is independently derived by Kirsch [3] using polar coordinates and by Muskhelishvili [4] using complex variable methods, as detailed by Timoshenko [5].

Beyond macroscopic geometric features, surface roughness also introduces stress concentrations that can significantly affect fatigue life. Neuber is the first to propose a model to quantify this effect [6]:

$$K_t = 1 + n\sqrt{\lambda \frac{R_z}{\rho}} \tag{2}$$

where $n$ is a factor dependent on the loading condition ($n = 1$ for shear, $n = 2$ for tension), $\rho$ is the notch root radius, and $\lambda$ relates the spacing to the height of the surface irregularities. Despite its age, Neuber's rule is still applied in contemporary research [7].

However, Neuber's formulation has been criticized for its applicability to certain materials, such as fiber reinforced plastics. Arola and Ramulu proposed an alternative formulation specifically for such materials [6]:

$$K_t = 1 + n\left(\frac{R_a}{\overline{\rho}}\right)\left(\frac{R_y}{R_z}\right) \tag{3}$$

This model incorporates standard surface roughness parameters, including the average roughness ($R_a$), peak-to-valley roughness ($R_y$), and ten-point mean roughness ($R_z$), as defined in [8]. The expression of 2D roughness parameters are the following:

$$\begin{aligned} R_a =& \frac{1}{L}\int_0^L |z| dx \\ R_y =& |z_{max} - z_{min}| \\ R_z =& \frac{1}{5}\left[\sum_{i=1}^{5}(z_i)_{max} + \sum_{j=1}^{5}|(z_j)_{min}|\right] \end{aligned} \tag{4}$$

where $z$ indicates the height of the rough profile, $L$ the evaluation length.

Subsequently, Arola extended the application of this model to metals, specifically AISI 4130 CR steel [8].

The theoretical stress concentration factor, $K_t$, assumes perfectly linear elastic material behavior. In reality, local plastic deformation at the notch root can mitigate the stress concentration. To account for this, the concept of the effective stress concentration factor, $K_{eff}$ (also known as the fatigue notch factor), is introduced. This factor is related to $K_t$ through the notch sensitivity, $q$, a material and geometry-dependent parameter determined experimentally [2] [9]:

$$K_{eff} = 1 + q(K_t - 1) \tag{5}$$

The utility of this relationship has been demonstrated in various studies, including by Arola for AISI 4130 CR steel [8] and by Lee et al. [10] for other materials.

Arola's formulation for $K_t$ has been adopted in subsequent research. For instance, Suraratchai et al. [11] integrated it into the Paris' law to model fatigue crack growth, thereby linking the stress intensity factor to the surface topography. Nevertheless, the general applicability of Arola's rule is limited by the relatively small number of materials for which it has been validated.

More recently, Zhang [7] conducted a critical assessment of Arola's rule using Finite Element Analysis (FEA). By virtually generating 41 specimens with varying surface roughness, Zhang found that Neuber's equation (2) provided a better prediction of the FEM-computed $K_t$ than Arola's original formula. Furthermore, Zhang proposed a new relationship, derived using a Bayesian learning approach, which showed a better fit to the FEM results:

$$K_t = 1.915\left(\frac{R_a}{R_y}\right)^{-0.223}\left(\frac{R_a}{R_z}\right)^{0.122}\left(\frac{R_a}{\rho}\right)^{0.549} \tag{6}$$

The aforementioned models are primarily applicable to two-dimensional profiles. For three-dimensional surfaces, other approaches have been developed. For example, Perz et al. [12] present an analytical model based on a Fourier series decomposition of the roughness profile under plane stress conditions, with

validation against FEM simulations. Persson [13] approached the problem by deriving the probability distribution of surface stress for randomly rough surfaces, leveraging the self-affine fractal nature of most surfaces.

This paper aims to evaluate the validity of common stress concentration factor formulas through a stochastic Finite Element Analysis. To this end, a series of 2D samples with statistically defined surface roughnessis generated. A robust meshing strategy, employing a surrogate-based optimization algorithm [14, 15] to control the Gmsh meshing library [16, 17, 18, 19], is used to ensure high-quality meshes that meet rigorous quality criteria. Subsequently, FEA is performed using Altair OptiStruct to compute the stress concentration factors. The numerical results are compared with predictions from the literature for various materials to assess the accuracy of existing models.

Table 1: Notation used in the present work

| Acronym | Meaning |
|---|---|
| $K_t$ | Stress Concentration Factor |
| $\rho$ | Local radius of curvature at the bottom of a valley |
| $\overline{\rho}$ | Average radius of curvature at the bottom of prominent valleys of a specimen |
| $R_a$ | 2D average roughness |
| $R_y$ | Peak-to-valley 2D roughness |
| $R_z$ | 10-point 2D roughness |

## 2 Methodology

This section details the computational framework developed for the analysis, encompassing the generation of specimen geometries with realistic surface roughness, the creation of high-quality finite element meshes, and the execution of the numerical simulations to determine stress concentration factors.

### *2.1 Specimen and Surface Roughness Generation*

A 2D dog-bone specimen is the baseline geometry of this analsis (Figure 1a). To simulate realistic surface conditions, a stochastic roughness profile is introduced onto one of the gauge section's edges. This profile is generated using a custom Python version of the 'rsgene1D.m' algorithm [20], which creates a one-dimensional random signal similar to a real roughness profile. The algorithm is specifically designed to produce a profile with a Gaussian height distribution and an exponential correlation function. The key statistical inputs controlling the generation process are:

- the Root Mean Square (RMS) height, that is the standard deviation of the surface heights, randomly set between 0 and 0.2 mm for each specimen.
- correlation length, that is the distance over which surface heights are correlated; this is fixed at 4 mm.

For each specimen, five concatenated rough segments were generated, creating a total rough edge length of 20 mm. The resulting geometry, with a detailed view of the rough profile, is illustrated in Figures 1b and 1c.

Following the generation of the rough surface, key roughness parameters ($R_a$, $R_y$, $R_z$) are calculated from the coordinates of the surface points according to the definitions in (4). A significant challenge in this process is the determination of the notch root radius, $\rho$, for the valleys in the roughness profile. Following the methodology established by Arola [6, 8] and also adopted by Lee et al. [10], the valley radius is determined by fitting a circle to at least three points within the lowest part of each valley, aiming to maximize the contact area. This graphical interpolation procedure is illustrated in Figure 2.

### *2.2 High-Fidelity Mesh Generation*

The accuracy of Finite Element Analysis (FEA) is intrinsically dependent on the quality of the computational mesh. In this work, a robust meshing procedure is implemented to ensure high-fidelity discretization of the 2D geometries. The open-source software Gmsh [16, 17] is employed via its Python API.

Recognizing that default meshing parameters rarely yield an optimal grid, a surrogate-based optimization algorithm [14, 15] is utilized to systematically determine the best meshing parameters. The

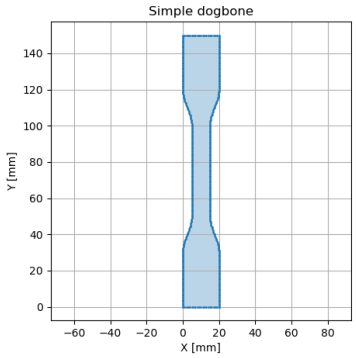


(a) Baseline dog-bone geometry with dimensions: gauge length = 50 mm, transition length = 20 mm, grip length = 30 mm, gauge width = 10 mm, grip width = 20 mm.

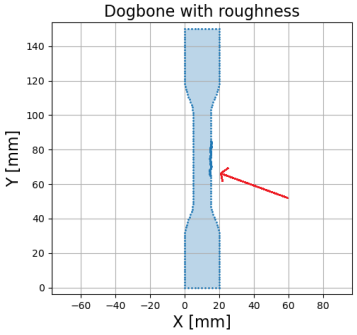


(b) Dog-bone specimen with a roughness profile applied to one side of the gauge section; the red arrow indicates the magnified area of Figure 1c

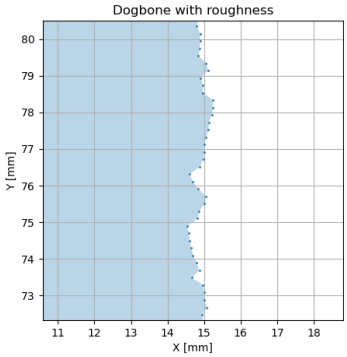


(c) A magnified view of the computationally generated surface roughness profile.

Figure 1: Geometries utilized in the Finite Element Analysis.

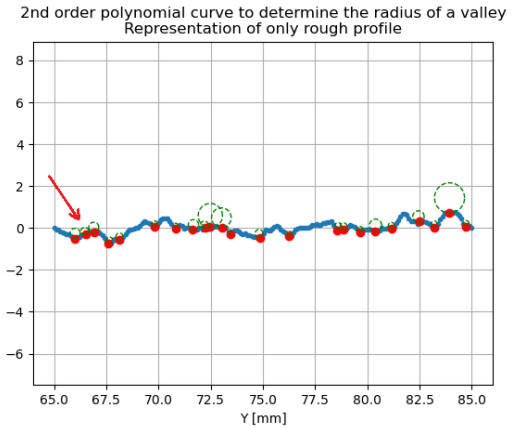


(a) Overview of circles fitted to the valleys of a roughness profile.

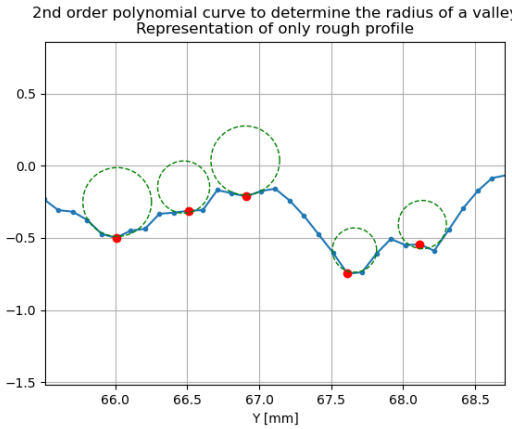


(b) Magnified view showing the detail of circle fitting at specific valleys.

Figure 2: Illustration of the procedure for calculating the notch root radius ($\rho$) by fitting circles to the most critical valleys in the rough profile.

optimization workflow, schematically shown in Figure 3, is driven by a multi-objective function designed to maximize mesh quality according to the criteria detailed in Table [2] from [21]. The objective function prioritizes quadrilateral (QUAD) elements over triangular (TRIA) elements to mitigate potential numerical inaccuracies, penalizing the presence of TRIA elements and enforcing stringent quality checks. Any mesh failing to meet the prescribed quality thresholds for a given specimen is automatically discarded. An example of a final mesh with applied boundary conditions is shown in Figure 4. The meshing algorithm refines the boundary by introducing nodes at a higher density than the points defining the initial geometry, ensuring a high-resolution discretization of the rough profile.

### *2.3 Solver*

The numerical simulations were performed using the commercial solver *Altair OptiStruct 2024.1*. An input file ('.fem') containing the mesh (CTRIA3 and CQUAD4 elements), material properties (thickness of elements 1mm), loads, and boundary conditions is generated programmatically and executed via a batch script.

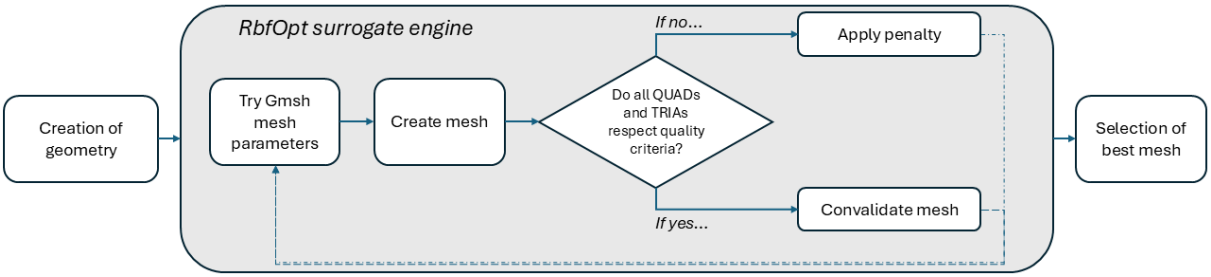


Figure 3: Schematic of the surrogate-based optimization algorithm used to find the optimal Gmsh parameters for generating a high-quality mesh.

Table 2: Quality Criteria for Triangular (TRIA) and Quadrilateral (QUAD) Elements [21].

| **Quality Metric** | **Description** | **Acceptance Limit** | **Ideal Value** |
|---|---|---|---|
| | **Triangular (TRIA) Elements** | | |
| Minimum Angle | Smallest internal angle. | $> 20°$ | $60°$ |
| Maximum Angle | Largest internal angle. | $< 120°$ | $60°$ |
| Aspect Ratio | Ratio of the longest edge to the shortest altitude. | $< 5$ | 1 |
| Jacobian | Measures deviation from an equilateral triangle. | $> 0.6$ | 1 |
| | **Quadrilateral (QUAD) Elements** | | |
| Minimum Angle | Smallest internal angle. | $> 45°$ | $90°$ |
| Maximum Angle | Largest internal angle. | $< 135°$ | $90°$ |
| Aspect Ratio | Ratio of the longest edge to the shortest edge. | $< 5$ | 1 |
| Jacobian | Measures distortion from a perfect square. | $> 0.6$ | 1 |

The analysis is configured as a 2D linear elastic simulation under plane stress conditions, assuming isotropic material behavior. As shown in Figure 4a, nodes on the bottom edge were fully constrained, while a uniform tensile load, resulting in a total force of 100 N in the vertical direction, is applied to the nodes on the top edge. The material properties for the aluminum alloy and steel used in this study are listed in Table [3].

Table 3: Isotropic linear elastic material properties used in the FEA.

| **Material** | **Young's Modulus, $E$ (MPa)** | **Poisson's Ratio, $\nu$** | **Source** |
|---|---|---|---|
| Aluminum Alloy | 72,000 | 0.33 | [7] |
| AISI 4130 CR Steel | 205,000 | 0.29 | [22] |

After the simulation run, the maximum Von Mises stress along the rough surface is extracted. The theoretical stress concentration factor, $K_t$, is then calculated by dividing this maximum stress by the nominal stress. The nominal stress is computed as the applied force (100 N) divided by the cross-sectional area of the gauge section (10 mm $\times$ 1 mm = 10 mm$^2$), resulting in a nominal stress of 10 MPa. This procedure is consistent with the method used by Zhang [7] for calculating $K_t$ from FEM results.

Figure 5 presents a typical Von Mises stress contour plot from the analysis.

## 3 Results

This section presents the results of the Finite Element Analysis, beginning with a mesh convergence study to establish the numerical stability of the proposed methodology. Subsequently, the stress concentration

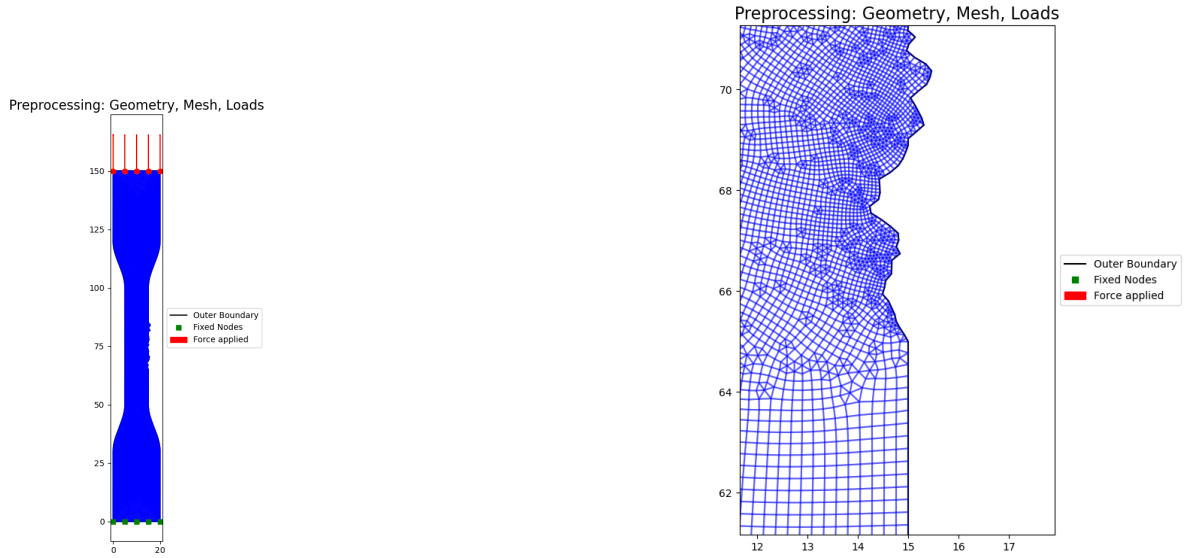


(a) Overview of the mesh and applied boundary conditions.

(b) A magnified view of the fine mesh along the rough boundary.

Figure 4: Example of a quality-approved mesh used for the FEA.

factors ($K_t$) computed from the simulations are compared against established analytical and empirical models from the literature for both aluminum and steel specimens.

### *3.1 Mesh Convergence Study*

A mesh sensitivity analysis is conducted to ensure that the numerical results are independent of the mesh discretization. 20 meshes are generated for the same geometry. Table [4] reports number of nodes in the rough border, average, maximum and minimum mesh size per each sample, where the size of one elements is estimated as the square root of the area. Figure 6 shows that the Stress Concentration Factor is constant and tends to an asymptotic value as the number of nodes on rough border increases, confirming the reliability of the numerical results obtained with the surrogate Gmsh procedure.

### *3.2 Analysis of Aluminum Specimens*

A set of 50 aluminum specimens with statistically varying surface roughness profiles is generated and analyzed. The FEM-computed $K_t$ values were then compared with the predictions from Arola's model [6] and Zhang's model [7], as illustrated in Figure 7.

The comparison reveals that for low stress concentration factors (approximately $K_t < 1.1$), Arola's rule shows good agreement with the FEM results. However, as the severity of the surface roughness increases, leading to higher $K_t$ values, Arola's model significantly underestimates the stress concentration observed in the simulations. This finding is consistent with the observations reported by Zhang [7]. In contrast, the Bayesian model proposed by Zhang, given by equation (6), demonstrates a much better correlation with the FEM results across the entire range of tested geometries. Nevertheless, a divergence in the trend is noticeable for higher $K_t$ values, which may be attributable to differences in the numerical methodologies or the specific roughness characteristics generated.

### *3.3 Analysis of Steel Specimens*

A similar analysis is performed for steel specimens. The computed $K_t$ values were compared against Arola's original rule and Zhang's rule. The results are presented in Figure 8.

For low $K_t$ values, a reasonable agreement is observed among the FEM results and the predictions from all three models. This aligns with the findings of Arola [8], where the model is validated in this low-$K_t$ regime. However, for more pronounced surface features corresponding to higher stress concentrations, both Arola's rule fails to accurately predict the FEM data. Notably, Zhang's rule, despite being originally developed for an aluminum alloy, provides a better prediction for the steel specimens over a wider range

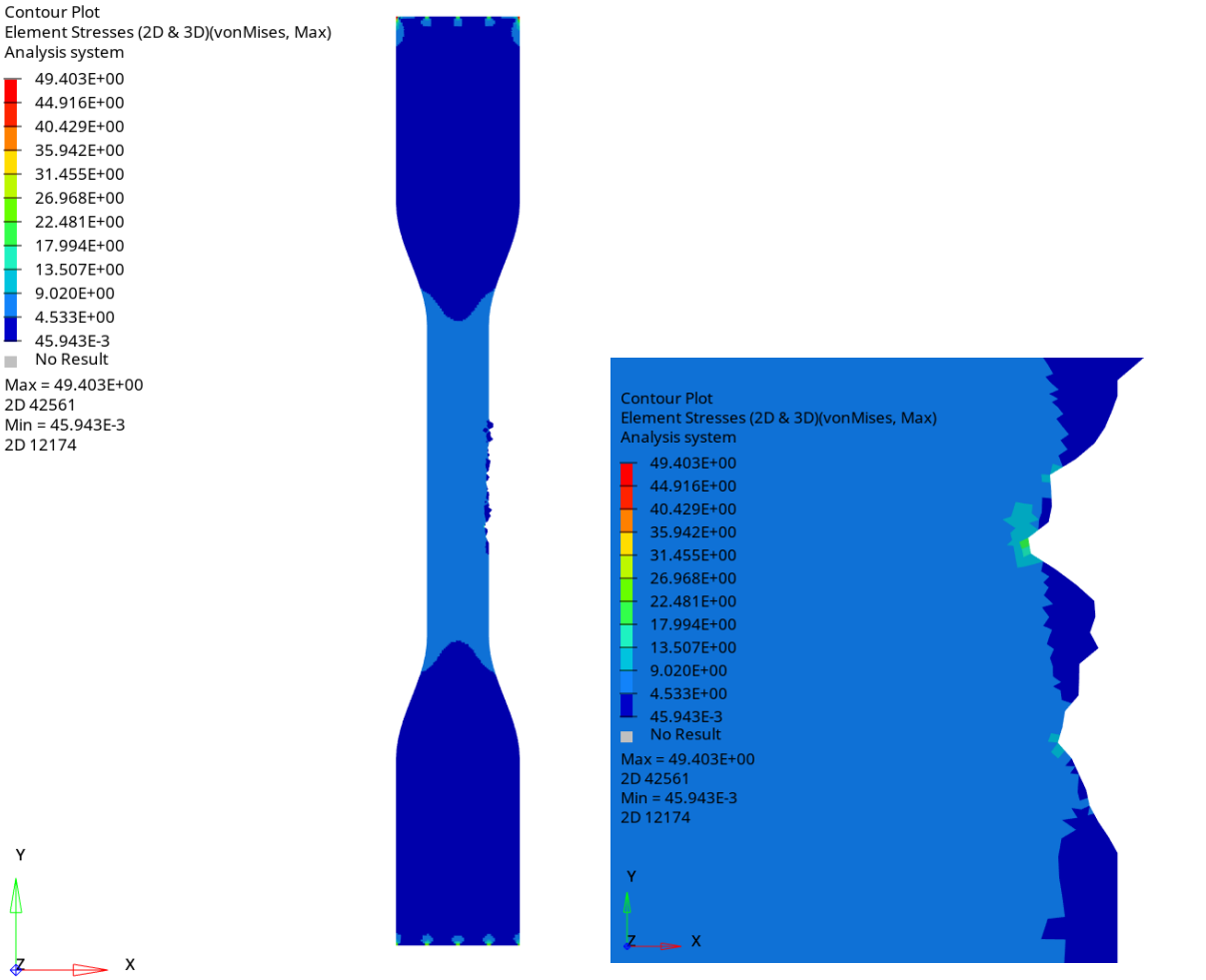


(a) Overall Von Mises stress distribution.

(b) Magnified view of stress concentrations in the valleys of the rough surface.

Figure 5: Example of Von Mises stress results for an Alluminium specimen under tensile load.

of $K_t$ values than the other models. This suggests that Zhang's formulation may capture the geometric effects of roughness more robustly, although its applicability should be further investigated for different material classes.

## 4 Discussion

This section discusses the methodological choices, interprets the observed trends, and contextualizes the findings within the existing literature.

### *4.1 Methodological Considerations*

In contrast to the rectangular geometry used by Zhang [7], this study employed a dog-bone specimen shape. This choice ensures a state of ideal uniaxial tension in the gauge section, by isolating the effect of surface roughness on the stress concentration factor, $K_t$, more effectively.

For mesh generation, the combination of a surrogate-based optimization algorithm with the Gmsh library proved to be highly efficient. It consistently produced high-quality meshes satisfying the criteria in Table [2] within a maximum of 50 iterations per sample. Alternative meshing tools like DistMesh [23] were considered but ultimately discarded. DistMesh is limited to generating triangular elements in 2D, which contradicts our goal of creating meshes dominated by higher-quality quadrilateral elements. Furthermore, preliminary tests indicated that Gmsh is computationally less expensive.

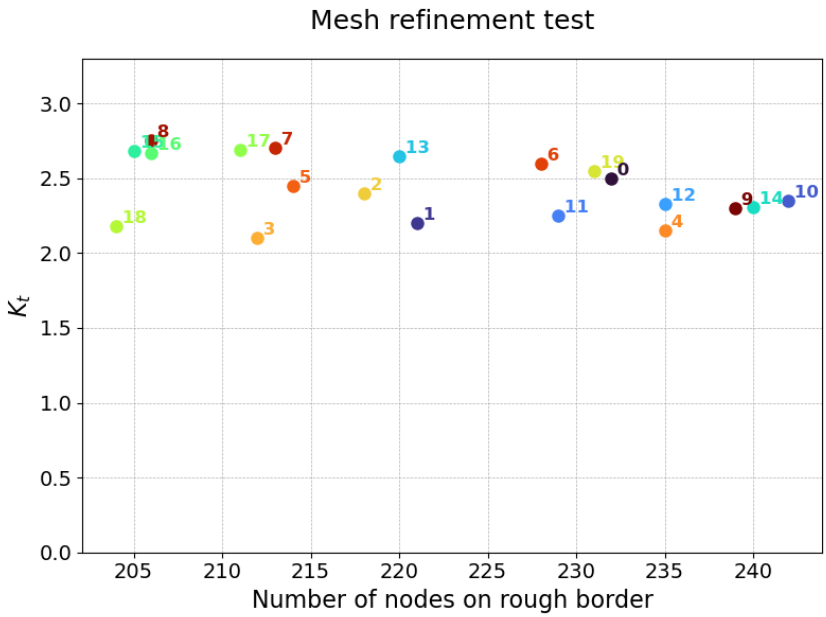


Figure 6: Number of nodes in rough border VS $K_t$

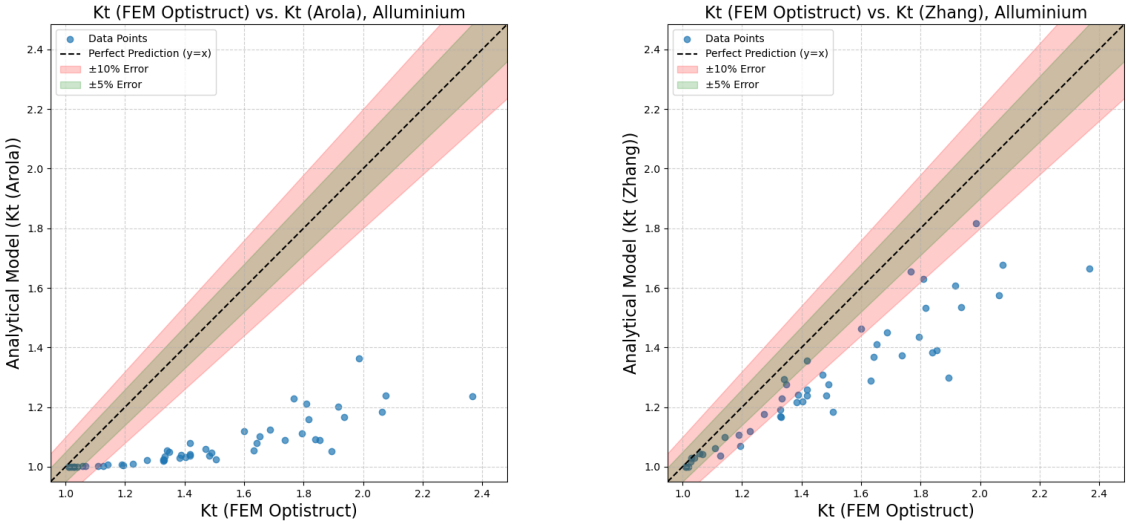


(a) Comparison with Arola's rule [6].

(b) Comparison with Zhang's rule [7].

Figure 7: Comparison of the stress concentration factor ($K_t$) computed via FEM with predictions from Arola's and Zhang's models for the 50 aluminum specimens.

It is important to note that the present analysis is strictly linear elastic. The applied load of 100N is deliberately kept low to ensure that even with stress concentrations, the peak local stress remained below the typical yield strength ($\sigma_y$) of both materials. With higher stress levels is necessary to perform a plastic analysis and use the correction for the effective stress concentration factor, $K_{eff}$. Future work should take into consideration that.

Table 4: Results of mesh sensitivity test

| Sample | Number of nodes in rough border | Avg. mesh size [mm] | Min mesh size [mm] | Max mesh size [mm] | Number of TRIAs | Number of QUADS |
|---|---|---|---|---|---|---|
| 0 | 232 | 0.335 | 0.053 | 0.558 | 3182 | 17279 |
| 1 | 221 | 0.181 | 0.052 | 0.292 | 4392 | 65542 |
| 2 | 218 | 0.234 | 0.053 | 0.386 | 3098 | 38883 |
| 3 | 212 | 0.147 | 0.052 | 0.237 | 2834 | 103380 |
| 4 | 235 | 0.148 | 0.047 | 0.244 | 7212 | 98475 |
| 5 | 214 | 0.236 | 0.054 | 0.374 | 1936 | 39410 |
| 6 | 228 | 0.326 | 0.051 | 0.521 | 2868 | 18775 |
| 7 | 213 | 0.341 | 0.052 | 0.622 | 1796 | 17971 |
| 8 | 206 | 0.343 | 0.052 | 0.576 | 1444 | 18127 |
| 9 | 239 | 0.232 | 0.054 | 0.363 | 4490 | 38125 |
| 10 | 242 | 0.237 | 0.052 | 0.391 | 4950 | 36130 |
| 11 | 229 | 0.180 | 0.048 | 0.305 | 6482 | 64601 |
| 12 | 235 | 0.232 | 0.054 | 0.378 | 4416 | 38158 |
| 13 | 220 | 0.337 | 0.052 | 0.619 | 2652 | 17594 |
| 14 | 240 | 0.232 | 0.055 | 0.351 | 4568 | 38057 |
| 15 | 205 | 0.334 | 0.050 | 0.626 | 1556 | 19058 |
| 16 | 206 | 0.334 | 0.051 | 0.624 | 1470 | 19106 |
| 17 | 211 | 0.334 | 0.052 | 0.625 | 1482 | 19107 |
| 18 | 204 | 0.172 | 0.051 | 0.255 | 1316 | 75990 |
| 19 | 231 | 0.327 | 0.053 | 0.514 | 3334 | 18202 |

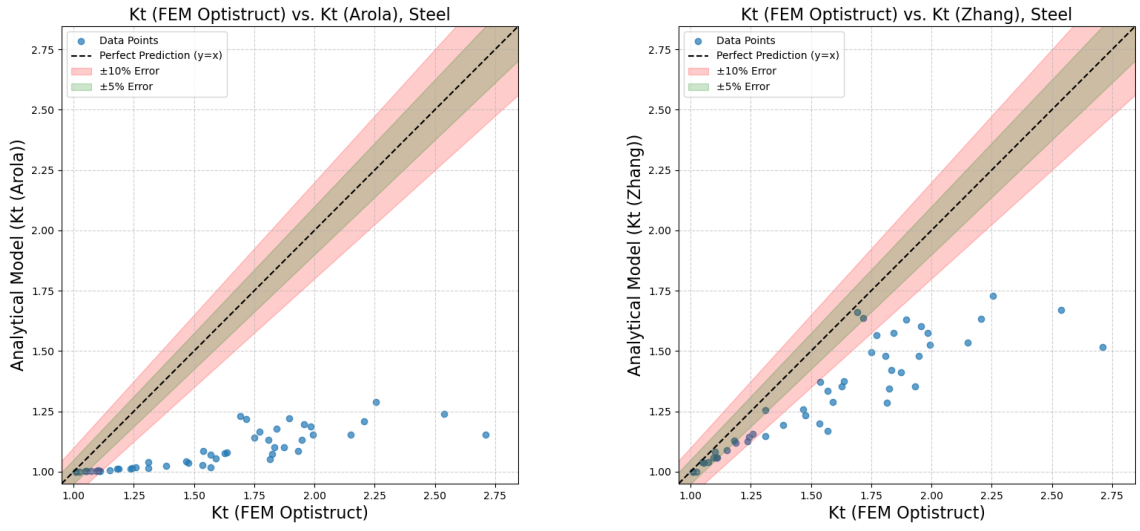


(a) Comparison with Arola's rule.

(b) Comparison with Zhang's rule.

Figure 8: Comparison of the stress concentration factor computed via FEM with predictions from Arola's rule and Zhang's rule for the steel specimens.

### *4.2 Influence of Roughness Parameters on $K_t$*

To understand the underlying mechanics, the influence of individual roughness parameters on the FEM-computed $K_t$ is investigated. The analysis included roughness values that exceed those typically found in as-built components to explore a wider design space.

As depicted in Figures 9 and 10, a clear positive correlation exists between $K_t$ and the roughness height parameters ($R_a$, $R_y$, and $R_z$) for both steel and aluminum. This aligns with established engineering principles, where smoother surfaces are specified to enhance fatigue resistance. Conversely, an inverse relationship is observed between $K_t$ and the average valley radius, $\overline{\rho}$. This is physically intuitive, as a smaller radius corresponds to a sharper notch, which produces a more severe stress concentration.

Second-order polynomial and reciprocal models were fitted to these relationships, with the resulting equations and coefficients of determination ($R^2$) summarized in Tables [5] and [6]. These tables provide quantitative models describing the sensitivity of $K_t$ to each geometric parameter for both the FEM results and the literature models.

### *4.3 Evaluation of Predictive Models*

In applications where surface roughness is minimal, leading to low stress concentration factors, the results suggest that most of the evaluated models, including Arola's rule, provide reasonable predictions. Given that many industrial components operate in this low-$K_t$ regime, the continued use of Arola's rule can be justified for its simplicity.

However, for components with higher surface roughness, Arola's rule shows significant deviation from the FEM results. Zhang's empirical model [7] demonstrates superior predictive accuracy across a broader range of roughness parameters for both materials investigated. Therefore, for applications where a more accurate prediction of $K_t$ is critical, Zhang's rule is recommended.

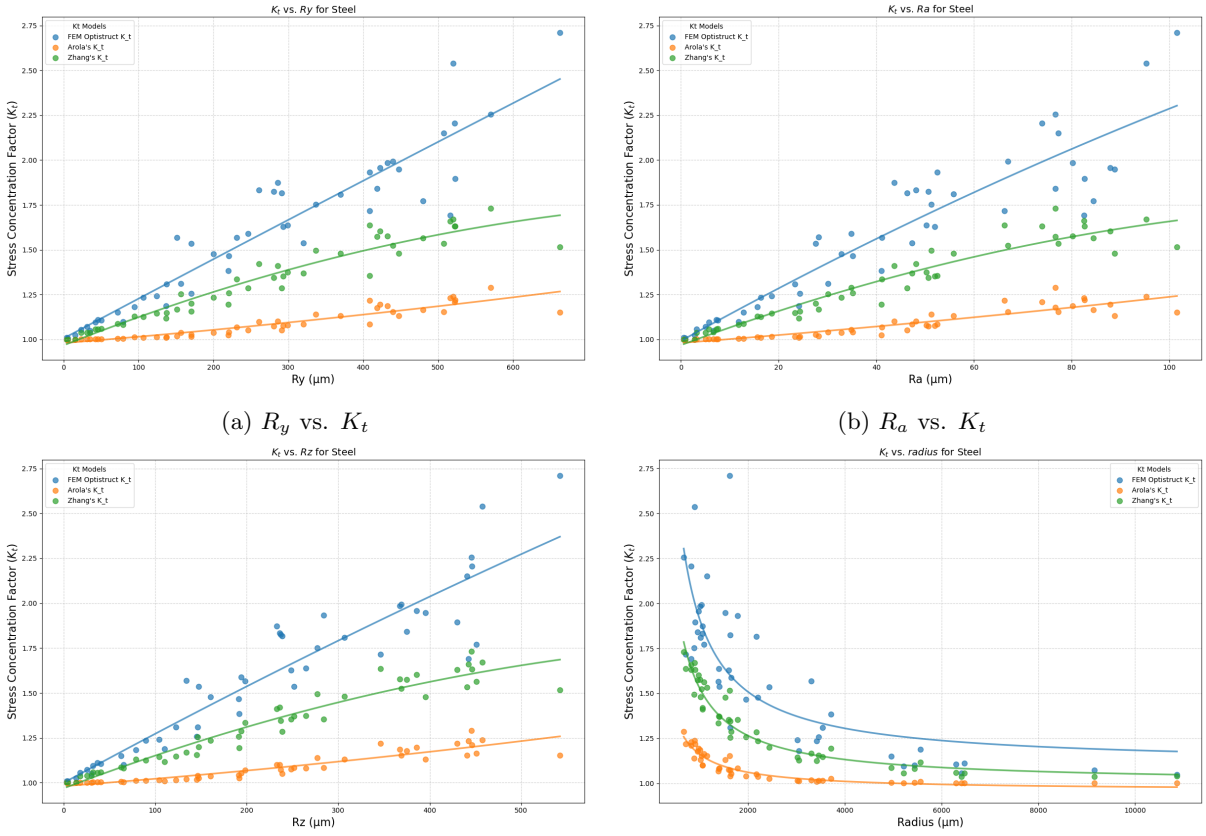


(a) $R_y$ vs. $K_t$

(b) $R_a$ vs. $K_t$

(c) $R_z$ vs. $K_t$

(d) $\overline{\rho}$ vs. $K_t$

Figure 9: Relationship between individual roughness parameters and the computed Stress Concentration Factor ($K_t$) for the steel specimens.

## 5 Conclusion

This study performed a systematic evaluation of common analytical and empirical models for the stress concentration factor ($K_t$) induced by surface roughness, using stochastic Finite Element Analysis. The

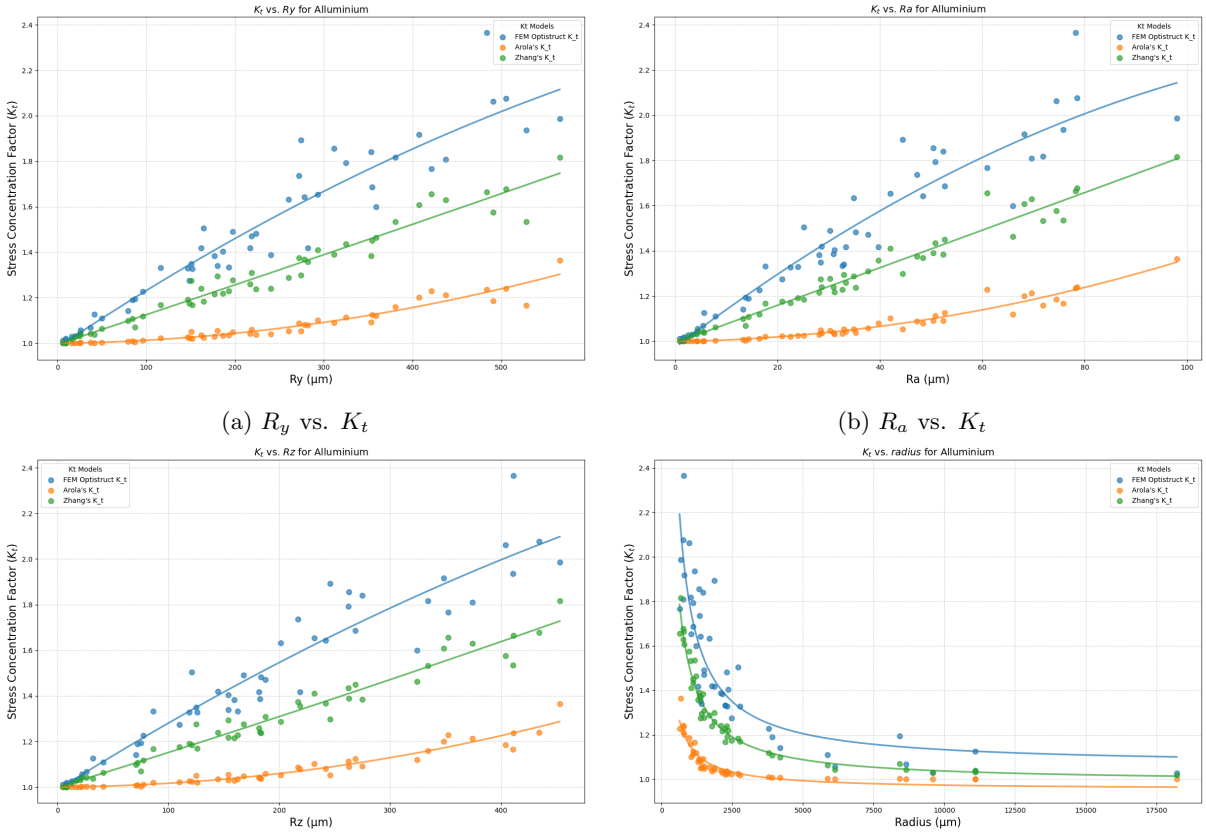


(a) $R_y$ vs. $K_t$

(b) $R_a$ vs. $K_t$

(c) $R_z$ vs. $K_t$

(d) $\overline{\rho}$ vs. $K_t$

Figure 10: Relationship between individual roughness parameters and the computed Stress Concentration Factor ($K_t$) for the aluminum specimens.

Table 5: Summary of regression models for Stress Concentration Factor ($K_t$) based on roughness parameters for Steel.

| **Parameter** | **Data Source** | **Fit Type** | **Equation** | $R^2$ |
|---|---|---|---|---|
| $R_a$ ($\mu$m) | FEM OptiStruct | Polynomial | $K_t = -2.13 \times 10^{-5} R_a^2 + 0.0151 R_a + 0.9915$ | 0.855 |
| | Arola's Model | Polynomial | $K_t = 4.65 \times 10^{-6} R_a^2 + 0.0021 R_a + 0.9803$ | 0.835 |
| | Zhang's Model | Polynomial | $K_t = -3.26 \times 10^{-5} R_a^2 + 0.0102 R_a + 0.9678$ | 0.923 |
| $R_y$ ($\mu$m) | FEM OptiStruct | Polynomial | $K_t = -5.69 \times 10^{-8} R_y^2 + 0.0022 R_y + 1.007$ | 0.884 |
| | Arola's Model | Polynomial | $K_t = 1.42 \times 10^{-7} R_y^2 + 3.39 \times 10^{-4} R_y + 0.9802$ | 0.853 |
| | Zhang's Model | Polynomial | $K_t = -8.50 \times 10^{-7} R_y^2 + 0.0017 R_y + 0.9676$ | 0.929 |
| $R_z$ ($\mu$m) | FEM OptiStruct | Polynomial | $K_t = -4.58 \times 10^{-7} R_z^2 + 0.0028 R_z + 0.9998$ | 0.870 |
| | Arola's Model | Polynomial | $K_t = 2.30 \times 10^{-7} R_z^2 + 3.86 \times 10^{-4} R_z + 0.9812$ | 0.860 |
| | Zhang's Model | Polynomial | $K_t = -1.13 \times 10^{-6} R_z^2 + 0.0019 R_z + 0.9693$ | 0.937 |
| $\overline{\rho}$ ($\mu$m) | FEM OptiStruct | Reciprocal | $K_t = 814.74/\overline{\rho} + 1.1024$ | 0.592 |
| | Arola's Model | Reciprocal | $K_t = 202.40/\overline{\rho} + 0.9606$ | 0.895 |
| | Zhang's Model | Reciprocal | $K_t = 532.56/\overline{\rho} + 0.9996$ | 0.925 |

key findings are as follows:

1. Arola's rule provides acceptable predictions for $K_t$ only in cases of low surface roughness. As

Table 6: Summary of regression models for Stress Concentration Factor ($K_t$) based on roughness parameters for Aluminum.

| **Parameter** | **Data Source** | **Fit Type** | **Equation** | $R^2$ |
|---|---|---|---|---|
| $R_a$ ($\mu$m) | FEM OptiStruct | Polynomial | $K_t = -5.79 \times 10^{-5} R_a^2 + 0.0177 R_a + 0.9639$ | 0.888 |
| | Arola's Model | Polynomial | $K_t = 3.27 \times 10^{-5} R_a^2 + 3.79 \times 10^{-4} R_a + 0.9982$ | 0.939 |
| | Zhang's Model | Polynomial | $K_t = 7.65 \times 10^{-7} R_a^2 + 0.0082 R_a + 0.9946$ | 0.960 |
| $R_y$ ($\mu$m) | FEM OptiStruct | Polynomial | $K_t = -1.14 \times 10^{-6} R_y^2 + 0.0027 R_y + 0.9746$ | 0.896 |
| | Arola's Model | Polynomial | $K_t = 8.60 \times 10^{-7} R_y^2 + 5.07 \times 10^{-5} R_y + 0.9985$ | 0.917 |
| | Zhang's Model | Polynomial | $K_t = 8.52 \times 10^{-8} R_y^2 + 0.0013 R_y + 0.9969$ | 0.950 |
| $R_z$ ($\mu$m) | FEM OptiStruct | Polynomial | $K_t = -1.39 \times 10^{-6} R_z^2 + 0.0031 R_z + 0.9853$ | 0.900 |
| | Arola's Model | Polynomial | $K_t = 1.35 \times 10^{-6} R_z^2 + 2.12 \times 10^{-5} R_z + 1.001$ | 0.926 |
| | Zhang's Model | Polynomial | $K_t = 2.95 \times 10^{-7} R_z^2 + 0.0015 R_z + 1.003$ | 0.958 |
| $\overline{\rho}$ ($\mu$m) | FEM OptiStruct | Reciprocal | $K_t = 721.35/\overline{\rho} + 1.0609$ | 0.750 |
| | Arola's Model | Reciprocal | $K_t = 197.64/\overline{\rho} + 0.9537$ | 0.882 |
| | Zhang's Model | Reciprocal | $K_t = 510.36/\overline{\rho} + 0.9860$ | 0.960 |

roughness increases, its accuracy diminishes significantly.

2. The Bayesian model proposed by Zhang demonstrated superior predictive capability over a wider range of roughness conditions for both aluminum and steel, making it a more robust choice for general engineering applications.

The present work has several limitations. The analysis is confined to a linear elastic material model and investigated only two materials. Furthermore, the roughness profiles were synthetically generated, without new experimental results.

Future research should be directed towards addressing these limitations. The inclusion of material plasticity in the FEM models would allow for a more rigorous investigation, also it could be compared to the value of the effective stress concentration factor, $K_{eff}$. Expanding the study to include a wider range of engineering alloys and incorporating experimentally measured surface profiles from real components would enhance the industrial relevance of the findings. Additionally, extending the framework to 3D analysis and investigating the influence of residual stresses and microstructural features would represent valuable contributions to the field. Finally, integrating these improved $K_t$ models into fatigue life prediction frameworks would be a logical next step.

## 6 Declarations

This publication is part of the project PNRR-NGEU which has received funding from the MUR–DM 117/2023

## References

[1] Schijve J 2009 *Fatigue of Structures and Materials* 2nd ed (Springer Dordrecht) ISBN 978-1-4020-6807-2

[2] Pilkey W D 1997 *Peterson's Stress Concentration Factors* (Wiley) ISBN 9780471538493

[3] Kirsch G 1898 *Zeitschrift des Vereines deutscher Ingenieure* **42** 797–807

[4] Muskhelishvili N I 1948 *Some Basic Problems Of The Mathematical Theory Of Elasticity* (Oxford University Press)

[5] Timoshenko S and Goodier J N 1970 *Theory of Elasticity* 3rd ed (McGraw-Hill)

[6] Arola D and Ramulu M 1999 *Journal of Composite Materials* **33** 102–123 (*Preprint* https://doi.org/10.1177/002199839903300201) URL https://doi.org/10.1177/002199839903300201

[7] Zhang J 2021 *Journal of Engineering Research and Reports* **21** 59–70 URL https://journaljerr.com/index.php/JERR/article/view/583

[8] Arola D and Williams C 2002 *International Journal of Fatigue* **24** 923–930 ISSN 0142-1123 URL https://www.sciencedirect.com/science/article/pii/S0142112302000129

[9] Boresi A P, Schmidt R J and Sidebottom O M 1993 *Advanced Mechanics of Materials* 5th ed (New York: John Wiley and Sons)

[10] Lee S, Pegues J W and Shamsaei N 2020 *International Journal of Fatigue* **141** 105856 ISSN 0142-1123 URL https://www.sciencedirect.com/science/article/pii/S014211232030387X

[11] Suraratchai M, Limido J, Mabru C and Chieragatti R 2008 *International Journal of Fatigue* **30** 2119–2126 ISSN 0142-1123 URL https://www.sciencedirect.com/science/article/pii/S0142112308001692

[12] Perez I, Madariaga A, Arrazola P, Cuesta M and Soriano D 2021 *International Journal of Mechanical Sciences* **190** 106040 ISSN 0020-7403 URL https://www.sciencedirect.com/science/article/pii/S0020740320320580

[13] Persson B 2023 *Tribol Lett* **71** URL https://doi.org/10.1007/s11249-023-01741-4

[14] Costa A and Nannicini G 2018 *Mathematical Programming Computation* **10** 597–629 URL https://doi.org/10.1007/s12532-018-0144-7

[15] Nannicini G 2021 *Open Journal of Mathematical Optimization* **2** 1–25 URL https://ojmo.centre-mersenne.org/articles/10.5802/ojmo.3/

[16] Geuzaine C and Remacle J F 2009 *International Journal for Numerical Methods in Engineering* **79** 1309–1331 URL https://onlinelibrary.wiley.com/doi/abs/10.1002/nme.2579

[17] Geuzaine C and Remacle J F Gmsh: a three-dimensional finite element mesh generator with built-in pre- and post-processing facilities https://gmsh.info/ last updated: May 24, 2024

[18] Remacle J F, Lambrechts J, Seny B, Marchandise E, Johnen A and Geuzaine C 2012 *International Journal for Numerical Methods in Engineering* **89** 1102–1119 URL https://doi.org/10.1002/nme.3279

[19] Remacle J F, Henrotte F, Carrier-Baudouin T, Béchet E, Marchandise E, Geuzaine C and Mouton T 2013 *International Journal for Numerical Methods in Engineering* **94** 494–512 URL https://doi.org/10.1002/nme.4458

[20] Bergström D 2010 rsgene1D.m: A 1D Random Surface Generator MySimLabs accessed: 2025-06-14 URL https://www.mysimlabs.com/surface_generation.html

[21] Gokhale N S, Thite A N, Deshpande S S and Bedekar S V 2008 *Practical Finite Element Analysis* (Finite To Infinite) ISBN 978-8190619516

[22] MatWeb Aisi 4130 steel, normalized at 870°c (1600°f) accessed: 2025-06-15 URL https://asm.matweb.com/search/specificmaterial.asp?bassnum=m4130r

[23] Persson P O and Strang G 2004 *SIAM Review* **46** 329–345 (*Preprint* https://doi.org/10.1137/S0036144503429121) URL https://doi.org/10.1137/S0036144503429121